Journal of
Materials Chemistry B

PAPER

View Article Online
View Journal | View Issue

Cite this: *J. Mater. Chem. B*, 2017, 5, 6376

Bio-inspired bioactive glasses for efficient microRNA and drug delivery

Xian Li,[abc] Qiming Liang,[ac] Wen Zhang,[ac] Yuli Li,[d] Jiandong Ye,[ac] Fujian Zhao,[ac] Xiaofeng Chen*[ac] and Shiren Wang*[b]

Received 13th April 2017,
Accepted 17th June 2017

DOI: 10.1039/c7tb01021d

rsc.li/materials-b

Bio-inspired pinecone-like bioactive glasses consisting of ordered thin-layers separated by consistent cavities were synthesized using a sol–gel process. The short diameter of the as-produced particles was as short as 161 nm, and the surface area was as high as 280 m^2 g^{-1}. The pore volume, ranging from $\sim$0.74 cm^3 g^{-1} to $\sim$0.67 cm^3 g^{-1}, could be modulated by the aqueous ammonia concentration. The surface was further tailored for positive charges by amino grafting. The as-produced nanoparticles could successfully enter cells *via* endocytosis. The microRNA delivery of the bioactive glass particles was further investigated by fluorescence microscopy and flow cytometry, indicating a loading efficiency and transfection efficiency greater than 90%. The potential of such particles as drug carriers was also studied. CCK8, live–dead cell staining and PI/annexinV double staining analyses confirmed that the bioactive glass particles loaded with antitumour doxorubicin (DOX) significantly accelerated the apoptosis of tumour cells. These bio-inspired bioactive glasses are promising as novel vectors for drug and microRNA delivery with high efficiency.

1 Introduction

Nature provides numerous diversity structures ranging from macroscale to microscale and nanoscale, and such fantastic structures inspire many interesting solutions to biomedical challenges. As an example, pinecones consist of ordered cone scales, which are separated by ordered cavities, and demonstrate high surface area and unique porosity for the efficient loading and release of pollen. Such a fantastic natural phenomenon inspired us to fabricate similar structures for the delivery of microRNAs and drugs.

MicroRNAs demonstrate great potential in modern medicine and therapies, but it is very challenging to deliver them to the desired location of tissues. Since two small regulatory RNAs, lin-4 and let-7, were revealed in 1993 and 2000, microRNAs have attracted great interest and related studies have been performed.[1,2] Human genomes contain at least a few hundred distinct microRNAs, and each microRNA is composed of $\sim$23 nucleotides (nt). As a class of noncoding RNA molecules, microRNAs regulate gene expression at the posttranscriptional level, and can bind to the 3′UTR sequences of mRNA and attenuate protein translation. Such microRNAs are small regulators, but play an important role in health and medical care.[1,2] MicroRNAs have demonstrated effective regulation of major signaling pathways, such as TGF-β (transforming growth factor-β), Wnt, Notch, p53, and mitogen-activated protein kinase (MAPK).[3] They also play important roles in developing and tailoring the responsiveness of cells to molecules that are directly associated with tissue morphogenesis and stem cell biology.[4,5] The role of microRNAs in several genetic diseases and other disease-related processes is also well established. In addition, emerging evidence also suggests a direct link between microRNAs and inflammation, as well as cancers.[6,7] MicroRNAs are often deregulated in cancer, including the loss of tumour-suppressive microRNAs and overexpression of oncogenic microRNAs.[6,7] MicroRNA-based anticancer therapies, either reconstituting tumour-suppressive microRNAs or depleting oncomiRs (oncogenic microRNAs) in cancer cells, represent an appealing strategy for cancer treatment. MicroRNAs have also been identified as a novel class of therapeutic agents for the treatment of other disorders,[8,9] and recently they have become potentially valuable therapeutic targets for gene therapy. However, the delivery of such microRNAs is very difficult.[10] The first barrier to overcome is the degradation and short half-life of microRNAs. Naked microRNAs are unstable when they are exposed to nucleases, and tend to degrade during both the synthesis process of bioengineering materials and subsequent

---

[a] *School of Materials Science and Engineering, South China University of Technology, Guangzhou 510641, People's Republic of China. E-mail: chenxf@scut.edu.cn*
[b] *Department of Industrial and Systems Engineering, Texas A&M University, College Station 77843, Texas, USA. E-mail: S.Wang@tamu.edu*
[c] *National Engineering Research Center for Tissue Restoration and Reconstruction, South China University of Technology, Guangzhou 510006, People's Republic of China*
[d] *Plastic Surgery Institute of Weifang Medical University, Weifang Medical University, Weifang 261042, People's Republic of China*

exposure to circulation serum. As a result, the delivery of microRNAs is extremely challenging. On the other hand, microRNAs have to be delivered into cells to take advantage of their functionalisation because they only function in the cytoplasm and cannot cross the cell membrane in the absence of transfection carriers.[9,10]

Some attempts have been made to deliver microRNAs *via* the viral method.[10] Despite good efficiency, viruses are not safe transfection carriers because of their severe immune/inflammatory reactions. Non-viral delivery using carriers such as liposomes, synthetic and natural polymers, and nanoparticles is an alternative approach. Liposomes (usually cationic) represent one of the most successful groups of gene vehicles. However, liposomes usually have poor physiological stability and are inactivated in the presence of serum. Polymer carrier systems, such as PEI, have the ability to buffer the acidic endosomal environment by the proton sponge effect and have demonstrated high transfection efficiency. However, some intracellular and extracellular cytotoxicity has been observed. Nanoparticle carriers, including nanoscale bioactive glasses (BGs), provide a method for the safe and efficient delivery of genes. They have the potential to protect genes from degradation and offer several advantages, including low immune toxicity, construction edibility, and facile fabrication.

BGs are important inorganic biomaterials that are mainly composed of SiO_2–CaO–P_2O_5. They can form a rapid, strong, and stable bond with host tissues,[11] and have been widely used in the field of soft and hard tissue repair and engineering.[11–14] They have demonstrated good biocompatibility, high bioactivity, and excellent bone restoration function.[13,15–17] Element-doped BGs or BG composites have also been thoroughly studied.[18–21] Mesoporous bioactive glasses (MBGs) at the nanoscale level have attracted much attention because of their special morphologies and physical–chemical properties.[22–24] They have many advantages, including high surface area and porosity, improved bioactivity, controllable morphologies and microstructure, controllable nanoparticle size, and a fast ion release rate. In addition, MBGs can also load and deliver biomolecules, such as chemical drugs and growth factors,[22,24–27] as well as DNA plasmid, which we first reported in 2014.[28,29] However, little work has been carried out to investigate the microRNA transfection function of MBGs.

Inspired by pinecones, we synthesized pinecone-like nanoparticles *via* a novel sacrificial liquid template method using the sol–gel process, and then tested the hypothesis that such novel bio-inspired MBGs could deliver microRNAs and drugs (Fig. 1). The nanostructure morphology-dependent delivery performance was examined.

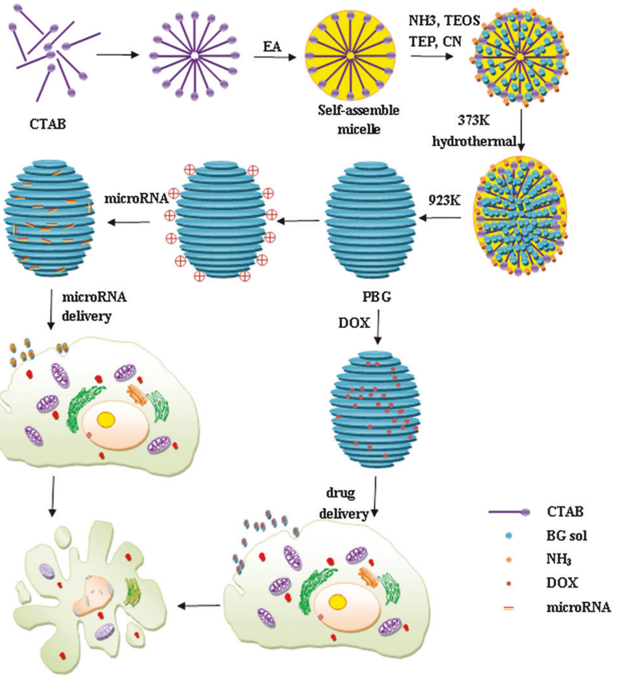

Fig. 1 Illustration of the synthesis of the PBGs for microRNA and drug delivery.

2 Materials and methods

2.1 Materials

Tetraethyl orthosilicate (TEOS), triethyl phosphate (TEP), calcium nitrate trahydrate(CN), ethanol absolute (EtOH), ethylacetate (EA), and ammonium hydroxide (NH_4OH) were purchased from the Guangzhou Chemical Reagent Factory (China). Hexadecyl trimethyl ammonium bromide (CTAB) was supplied by Aladdin (Shanghai, China). All of the above chemical reagents were of analytical grade. Deionized water (DW) was obtained from a water purification system (Milipore S.A.S., France). Doxorubicin (DOX) was provided by Sigma Co. (USA). A human Hela cell line was preserved by our laboratory. Dulbecco's modified Eagle's medium (DMEM), trypsin, and fetal bovine serum were obtained from Gibco Co. (USA). The CCK8 kit was from Dojindo Molecular Technologies Inc. (Japan). All the microRNAs were purchased from Genepharma Co. (Shanghai, China). Lipofectamine™ 2000 was purchased from Invitrogen (Carlsbad, CA, USA). Lyso-Tracker Red and DAPI were purchased from the Beyotime Institute of Biotechnology (Jiangsu, China). An Annexin V-FITC/PI Apoptosis Detection Kit was obtained from BestBio (Shanghai, China).

2.2 Preparation of bioactive glass nanoparticles

Small and big bioactive glass particles (70 mol% SiO_2, 30 mol% CaO, 70S30C) with pinecone structures, PBGs-1 and PBGs-2, were prepared as described in our previous article.[30] The processes were as follows using EA–CTAB–water micro-emulsion droplets as a soft template: first, 0.7 g CTAB was dissolved in deionized water (DW, 33 mL) under stirring. Then, 10 mL of EA was added to the above solutions. After stirring for 30 min, micro-emulsion droplets were obtained. Then, 7 mL of aqueous ammonia was added dropwise to the solution and hydrolysed for 30 min at room temperature. The concentrations of the aqueous ammonia added during the synthesis of PBGs-1 and PBGs-2 were 3 and 5 mol L^{-1}, respectively. The mixture was stirred for 15 min, and 3.6 mL TEOS, 0.36 mL TEP, and 2.277 g CN were sequentially added at 30 min intervals. The mixture was stirred for another 30 min and transferred into a Teflon-lined autoclave. The mixture was heated at 373 K for 20 h under autogenous pressure. Then, the white precipitate was collected by centrifugation, washed three times with EtOH and DW in turn, dried at 333 K, and calcined at 923 K under air (Fig. 1).

Transmission electron microscopy (TEM) images of the PBGs were obtained by TEM using a JEM-2100HR microscope with an accelerating voltage of 100 kV. The SEM images were recorded using a ZEISS Merlin microscope at an accelerating voltage of 5 kV.

Mineralization of the nanoparticles: nanoparticles were soaked in simulated body fluid (SBF) (1.0 mg mL^{-1}) and placed in a shaking incubator. After soaking for 3 days, the samples were collected, rinsed, and then dried. The apatite formed on the surface was characterised using SEM.

2.3 PBGs–NH$_2$ system

Amino-modified PBGs (PBGs–NH$_2$) were synthesized following the protocol we have reported previously, and the zeta potential was measured.[24] All experiments were performed in triplicate.

2.4 MicroRNA preparation

Human miR-7 sequence was obtained from the miRBase Sequence Database (http://www.mirbase.org). The sense strand sequence was as follows: hsa-miR-7-5p, 5′-UGGAAGACUAGUGA UUUUGUUGU-3′. The double-stranded miR-7 mimics (miR-7), miR-7 chemically modified with FAM (miR-7–FAM), and negative control microRNAs with random sequence (NC) were all purchased from Genepharma Co. (Shanghai, China).

2.5 MicroRNA loading efficiency

The buffer of the agarose gel electrophoresis was prepared with DEPC water. The prepared microRNAs were supplemented with sterilized DEPC water to adjust the final concentration of the microRNAs to 20 nM. The PBGs–NH$_2$ were mixed with miR-7 (1 μL) at different ratios (0, 20, 40, 80, 100, and 200). The total volume of the reaction system was 100 μL. The complex was incubated for 30 min at room temperature, and then 20 μL of the mixture was taken out to detect the loading efficiency by agarose gel electrophoresis.

To determine the microRNAs loading efficiency by flow cytometry, different amounts of PBGs–NH$_2$ were mixed with miR-7-FAM. PBGs–miR-7–FAM was collected by centrifugation at 10 000 rmp for 5 min and then re-suspended in DEPC water. The fluorescence of miR-7–FAM in the nanoparticles was measured by flow cytometry.

2.6 Cell localization and transfection efficiency of PBGs-microRNA

PBGs–NH$_2$ nanoparticles were incubated with miR-7–FAM for 30 min at room temperature to form a PBGs–NH$_2$/miR-7–FAM (50 : 1) complex. Cells cultured in 6-well plates were incubated with the complex (50, 75, 100 μg mL^{-1}) for 4 h. After transfection for 24 hours, some cells were washed with PBS twice, and examined under fluorescence microscopy to observe the localization of PBGs in the cells. Other PBGs–NH$_2$/miR-7–FAM incubated cells were digested, collected, and detected by flow cytometry to determine the transfection efficiency.

After incubation with PBGs–NH$_2$/miR-7–FAM for 4 h in 5% CO$_2$ incubator, Hela cells cultured in special confocal dishes were washed with PBS and fixed with 500 μL 4% (w/v) formaldehyde for 30 min. Cells were washed with PBS twice and incubated with 300 μL Lyso-Tracker Red dye for (50 nM) 50 min at 37 °C. Cells were washed and incubated with 300 μL DAPI nuclear staining for 5 min, washed again by PBS, and then observed using a laser confocal fluorescence microscope.

2.7 PBGs/DOX system

Some 10 mg PBGs sterilized by autoclaving were soaked in 5 mL 100 μg mL^{-1} DOX–PBS solution (sterilized through the 022 μM membrane) separately and put into a shaker at 4 °C overnight. The nanoparticles were centrifuged at 10 000 rpm for 10 min, and the supernatants were completely removed. Then, 5 mL phosphate buffered saline (PBS) was added to the nanoparticles and centrifuged again. DOX-loaded nanoparticles were collected. The loading amount of DOX was determined by a multimode microplate reader (Thermo, Varioskan Flash) at a wavelength of 480 nm to calculate the difference in the DOX concentration in the PBS before and after loading. Encapsulation efficiency (%) = [(initial DOX amount − supernatant DOX amount after loading experiment)/initial DOX amount] × 100%. For the DOX release test, the collected PBGs–DOX nanoparticles were soaked in 10 mL fresh PBS in a 37 °C shaker for different periods of time. At each time point, 1 mL PBS solution was taken out to measure the released DOX, and 1 mL fresh PBS was added back in. The accumulative release percentage of DOX from the nanoparticles was calculated. The supernatant DOX amount of the first measurement was recorded as M_1, and that of the Nth measurement was recorded as M_N. The release equation of the first measurement was as follows: releasing efficiency (%) = [M_1/(initial DOX loading amount) × (encapsulation efficiency)] × 100%. The release equation of the second measurement was as follows: releasing efficiency (%) = {[(1/10) × M_1 + M_2]/[(initial DOX loading amount) × (encapsulation efficiency)]} × 100%. The release equation of the Nth measurement was as follows: releasing efficiency (%) = {[(1/10) × M_1 + (1/10)M_2 + ⋯ + (1/10)M_{N-1} + M_N]/[(initial DOX loading amount) × (encapsulation efficiency)]} × 100%. All experiments were performed in triplicate.

2.8 Cell culture and proliferation assay

Hela cells were cultured in DMEM medium supplemented with 10% fetal bovine serum, at 37 °C in a 5% CO$_2$ incubator. The effect of the PBGs and PBGs/DOX on the proliferation of the cells was determined using the CCK8 assay. Cells cultured in 96-well plates were treated with different PBGs or PBGs/DOX for 48 h at 37 °C. A 10 μL volume of CCK8 was added to each well and the cells were incubated for another 4 h. The absorbance was measured at 450 nm using a microplate reader (Thermo 3001, Thermo Co., USA). Three specimens for each culture time point were tested and each test was performed in triplicate.

2.9 Live–dead cell staining

Hela cells were cultured in 24-well plates, and incubated with different PBGs/DOX for 48 h. Cells were washed with PBS twice, then 100 μL of live–dead cell staining assay solution was added to each well. Cells were incubated at 37 °C for 60 min. The fluorescence was detected using a fluorescence microscope. Calcein-AM only stains viable cells to emit strong green fluorescence. Propidium iodide (PI), a nucleus staining dye, interacts with dead cells to emit red fluorescence.

2.10 Annexin V/PI apoptosis detection

Cells were cultured in 24-well plates for 24 h. PBGs/DOX nanoparticles were added and incubated for 48 h, and then collected and centrifuged at 1000 rpm for 5 min. The supernatant was discarded and the cells were resuspended in 50 μL DMEM. 50 μL of annexin V/PI working solution was added to each of cell suspension. The cells were incubated at room temperature for 20 min. As soon as possible, the stained cells were analysed by flow cytometry.

2.11 Statistical analysis

Data are represented as means ± SD for the absolute values. Statistical results were obtained using the statistical software SPSS 17.0. A two-sample *t*-test was used for statistical analysis. Values of $P < 0.05$ were considered significant.

3 Results and discussion

3.1 Properties of BG particles

In this work, pinecone-like bioactive glass nanoparticles (PBGs) were fabricated in colloidal solution. Surfactant CTAB was tuned to a specific layered micelle by controlling the concentration, and then a template-assisted *in situ* reaction and hydrothermal process resulted in the pinecone-like nanostructures. In this synthesis process, the Hexadecyl trimethyl ammonium bromide (CTAB) micelle was self-assembled with ethylacetate (EA) to form O/W micro-emulsion droplets, which worked as the template. Aqueous ammonia was used as a catalyst and template corrodent. When BG sol was added, the micro-emulsion droplet template corroded and the BG gel formed at the same time. As the temperature and pressure increased, the arrangement of the CTAB gathered at the oil–water interface was disturbed and reset, which resulted in a different corroding path and presented lamellar structure. The whole nanoparticle was composed of many inter-connected nanosheets. The size of the nanoparticles was modulated by changing the aqueous ammonia concentration, resulting in two different nanoparticles, small pinecone bioactive glasses (PBGs-1), and big pinecone bioactive glasses (PBGs-2).

The as-produced nanostructures were also characterized by high-resolution TEM, as shown in Fig. 1. The obtained PBGs exhibited pinecone-like morphology. The shortest diameters for PBGs-1 and PBGs-2 were 161 ± 14 nm and 193 ± 13 nm, respectively. The TEM images of PBGs-1 and PBGs-2 (Fig. 2) showed that the nanoparticles were composed of ordered cavity-separated thin layers, which demonstrated a thickness of around ~2 nm. All the nanoparticles exhibited type IV isotherm patterns with H3-type hysteresis loops.[26] The average pore diameter increased with the aqueous ammonia concentration. PBGs-2 contained larger pores (average pore diameter: 14.0356 nm) with a wider size distribution than PBGs-1 (average pore diameter: 10.5092 nm). The Brumauer–Emmett–Teller surface area of PBGs-1 (280.221 $m^2\ g^{-1}$) was much larger than that of PBGs-2 (191.972 $m^2\ g^{-1}$). The average total pore volumes of the two kinds of nanoparticles, PBGs-1 and PBGs-2, were very similar (0.7362 and 0.6736 $cm^3\ g^{-1}$, respectively).

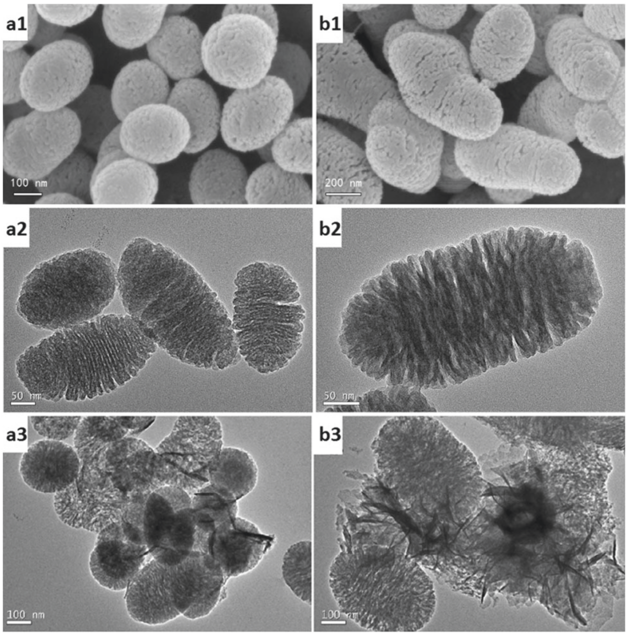

Fig. 2 SEM micrographs and TEM images of PBGs-1 (a1 and a2) and PBGs-2 (b1 and b2), and TEM images of PBGs-1 (a3) and PBGs-2 (b3) after soaking in SBF for 3 days.

We successfully synthesized many kinds of MBGs with different morphologies, such as spherical,[31] radial,[28] hollow,[32] and mono dispersive MBGs.[33–35] Such pinecone-like nanostructures have unique morphology and may be promising for the delivery of microRNAs or drugs due to their structures and porosity. The nanoparticles possessed excellent apatite-mineralization formation properties (Fig. 2). After being immersed in simulated body fluid (SBF) for 3 days, a mineralized layer was formed on the surface of the nanoparticles, and the HA was flaky.

Although sol–gel/block copolymers and surfactant methods are simple, increasing the CaO content resulted in irregular morphology of the particles from their natural state.[36,37] It is not easy to maintain the calcium concentration and the morphology of particles at the same time. In this study, the chemical components were also characterized (Fig. 3). The element O, Si,

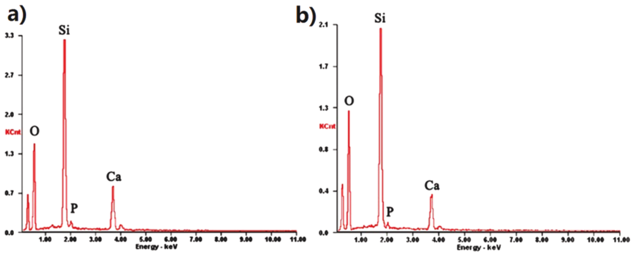

Fig. 3 Element composition of PBGs-1 (a) and PBGs-2 (b).

P, Ca emission peaks indicated that P and Ca elements successfully entered the Si–O network. The particles contained 1–2 mol% P, 11–12 mol% Ca, and about 87 mol% Si. The actual content of P and Ca was much smaller than that of the original design. Because Ca^{2+} has strong water solubility, part of Ca^{2+} remained in the reaction liquid. The centrifuged and rinsed steps during the synthesis process also took away some Ca^{2+}.

3.2 Zeta potential characterization and miR-7 loading efficiency

Next, we chose PBGs-1 to study the microRNA and drug delivery because of its smaller size. The zeta potentials of PBGs and PBGs–NH_2 were also measured to understand the surface charge of the nanoparticles. As shown in Table 1, PBGs-1 had a negative zeta potential of −16.63 mV in neutral water because of the dissociation of the surface silanol groups. Further amination of the nanoparticles significantly increased the zeta potential, and thus could significantly improve the loading efficiency.

MiR-7 was selected for this study because it is the most reduced microRNA in cancer stem-like cells and directly targets and down-regulates central oncogenic factors in cancer-associated signaling pathways, including EGF receptor, IRS-1, IRS-2, Pak1, Raf1, Ack1, and PIK3CD. The effective delivery of miR-7 is very important for tumour-suppressive purposes.[38] In this study, the miR-7 loading efficiency of PBGs was examined by gel electrophoresis. As shown in Fig. 4, miR-7 was added to different amounts of nanoparticles separately. When the mass ratio of PBGs-1–NH_2/microRNAs = 0, microRNAs only could be seen in the gel. When the mass ratio of PBGs-1–NH_2/microRNAs = 20 or 40, microRNAs could be detected both in the gel and in the sample holes, because some of the microRNAs were loaded by the nanoparticles and some were free. As the ratio increased, microRNAs only were detected in the sample hole, which indicated that all the microRNAs were combined with PBGs-1–NH_2. The surface of the PBG nanoparticles and the microRNAs all had negative charge. Although the microRNAs could be loaded by BG particles because of their small size, PBG nanoparticles were modified by amino groups to reduce repulsion between the particles and microRNAs. The microRNA loading of the nanoparticles may be different from the plasmid DNA loading that we reported before. Plasmid DNA always contains several kilobase pairs, which is much larger than microRNAs, so the loading of plasmid DNA mainly depends on the electrostatic interaction of the plasmid and the nanoparticles.[28,29] MicroRNAs are much smaller and have the possibility of entering the mesopores of the PBGs. The specific surface area of the nanoparticles may also have been one of the main essential factors affecting the microRNA loading.

Table 1 Zeta potential of PBGs in pure water

Nanoparticles	Zeta potential (mV)
PBGs-1	−16.63 ± 0.81
PBGs-1–NH_2	+0.17 ± 0.15

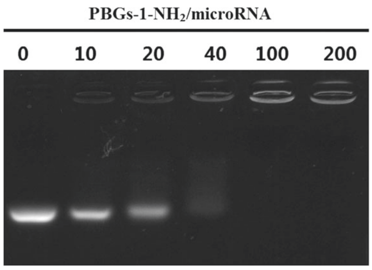

Fig. 4 MicroRNA loading efficiency of PBGs-1–NH_2 characterized by gel electrophoresis.

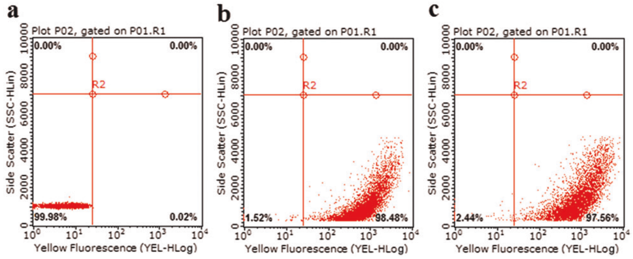

Fig. 5 miRNA loading efficiency of PBGs–NH_2 tested by flow cytometry. (a) PBGs-1–NH_2; (b) PBGs-1–NH_2/miRNA ratio = 40 : 1; (c) PBGs-1–NH_2/miRNA ratio = 80 : 1.

The miR-7 loading efficiency of PBGs was also studied by flow cytometry. Specifically, miR-7 was functionalized with fluorescent groups so as to be detectable in the flow cytometry. As shown in Fig. 5, the scatter diagram of experimental groups moved to the right more obviously when compared with the control. The miR-7–FAM labelling efficiency of PBGs-1–NH_2 was above 90% when the PBGs–NH_2/microRNA ratio was 40 or 80. The nanoparticles could interact with microRNA with high efficiency.

3.3 Transfection of miR-7

The transfection of miR-7 was also studied. Appropriate nanoparticle/microRNA proportions are required for effective cell transfection. Excessive microRNAs could lead to large waste, while fewer microRNAs could lead to increased cytotoxicity due to the extra positive charges contributed by the nanoparticles. According to the gel electrophoresis results, the appropriate ratio range was from 40 : 1 to 100 : 1. To determine whether the PBG nanoparticles could successfully enter the cells, and to investigate the effect of their concentrations on cells, Hela cells were co-cultured with PBGs–NH_2/miR-7–FAM nanoparticles at different concentrations. A fluorescence microscope was used to determine the localisation of the nanoparticles in the cells. Fig. 6 showed that after 4 h incubation, most of the PBGs–NH_2/miR-7–FAM nanoparticles were in cells, indicating that the nanoparticles could enter the cells successfully. More than 90% of cells could be tested for the FAM fluorescence intensity by flow cytometry (Fig. 6) in the experiment groups, which was higher than that of commercial liposome reagent. The 75 $\mu g\ mL^{-1}$ experimental groups had higher positive expression than the 50 $\mu g\ mL^{-1}$ groups. When the concentration increased to 100 $\mu g\ mL^{-1}$, it seemed that the cells were not in a good state

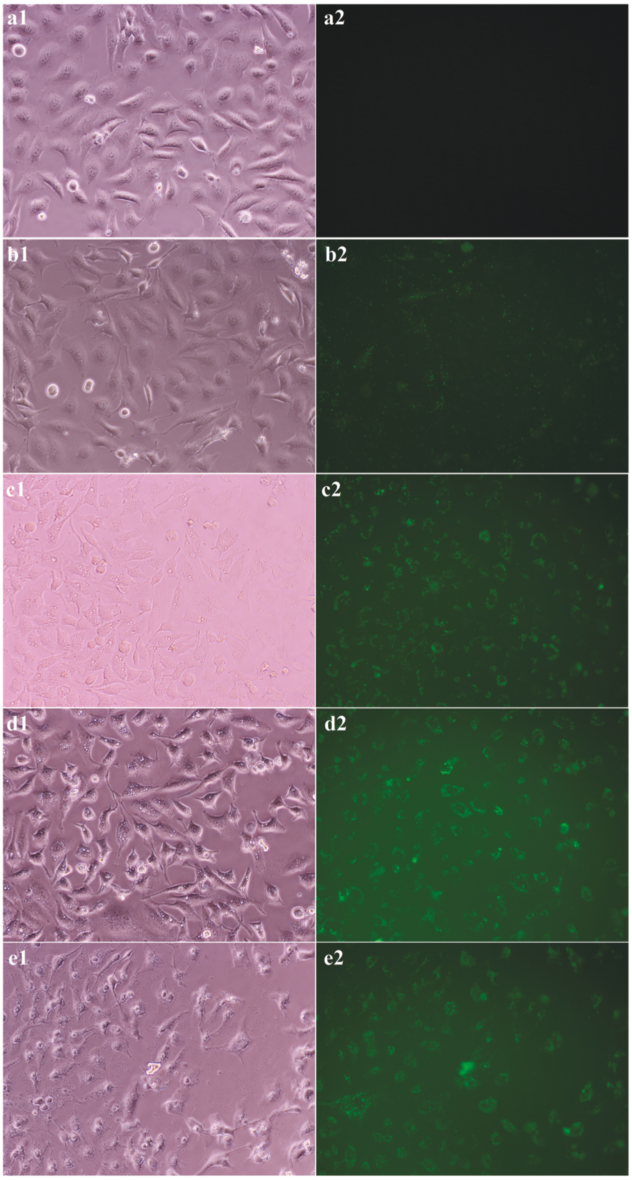

Fig. 6 Fluorescence microscopy images and fluorescence intensity of Hela cells after incubation with PBGs-1–NH_2/miR-7–FAM (50 : 1). (200×) (a) control; (b) Lipofectamin 2000; (c–e) 50, 75 and 100 μg mL^{-1} PBGs-1–NH_2/miR-7–FAM; left column: light microscopy; right column: miR-7–FAM.

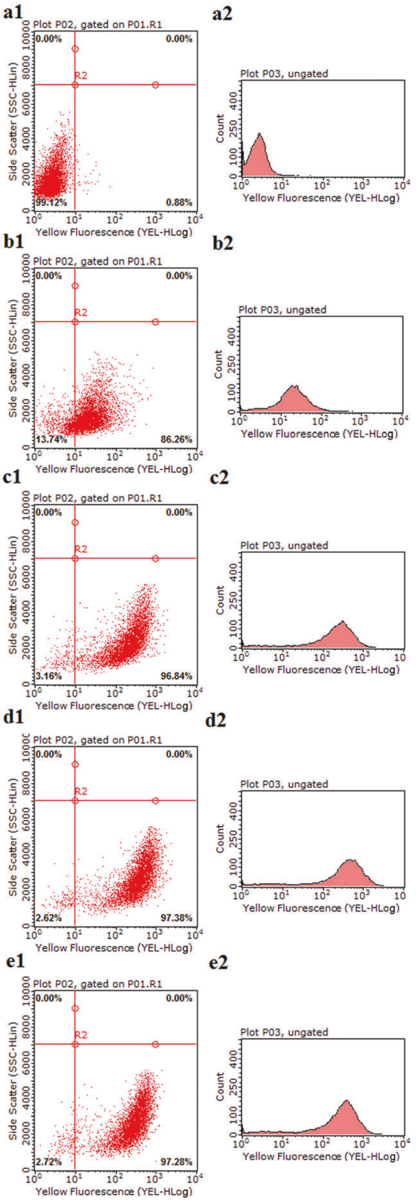

Fig. 7 Expression of miR-7–FAM in Hela cells tested by flow cytometry. (a) control; (b) Lipofectamine 2000; (c) PBGs-1–NH_2/miR-7–FAM 50 μg mL^{-1}; (d) PBGs-1–NH_2/miR-7–FAM 75 μg mL^{-1}; (e) PBGs-1–NH_2/miR-7–FAM 100 μg mL^{-1}.

and many of them became irregular (Fig. 6), although the positive expression rate was still above 95% (Fig. 7). The optimal transfection concentration was found to be under 100 μg mL^{-1}. In comparison, little fluorescence was detected in the control group.

Furthermore, a confocal laser scanning microscope was used to determine the localization of the nanoparticles in the cells. Blue DAPI was used to show the nucleus; green FAM showed the localization of the PBGs–NH_2/miR-7–FAM; and Red Lyso-tracker showed the lysosomes. When the PBGs–NH_2/miR-7–FAM ratio was 50, and the concentration was 50 μg mL^{-1}, their spatial locations were examined, as shown in Fig. 8. PBGs-1–NH_2/miR-7–FAM successfully entered the cells while most of them were in the cytoplasm. No nanoparticles were observed in the nucleus. A large number of red lysosome dots were observed in the cytoplasm, and their localizations were not all consistent with those of PBGs–NH_2/miR-7–FAM, indicating that some of the nanoparticles could escape from the lysosomes. Because of [Ca^{2+}] ion dissolution products released from the BGs,[39,40] they may result in allowing transfecting agents to escape the phagocytic pathway and promote gene expression in the cells.

3.4 DOX loading efficiency

As described earlier, the PBGs exhibited good microRNA loading ability. The PBGs possessed a unique pore structure and large surface area, which provided the nanoparticles potential applications as delivery carriers of drugs. The loading and releasing

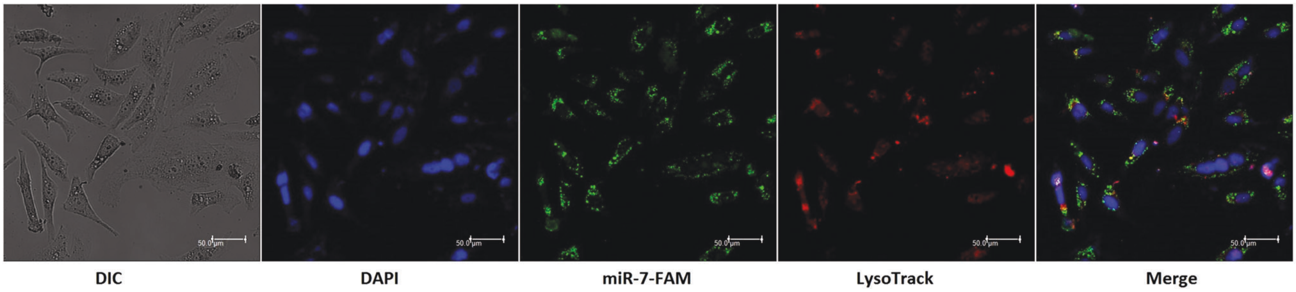

Fig. 8 Images of Hela cells after incubation with PBGs-1-NH_2/miR-7-FAM detected by a laser scanning confocal microscope. Scale length = 50 μM.

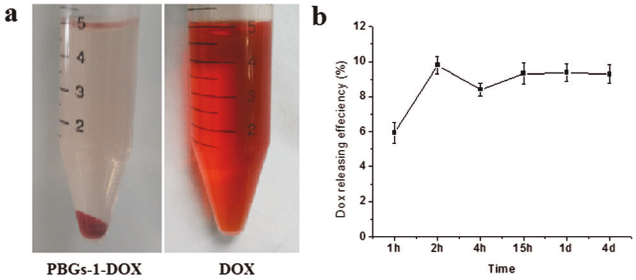

Fig. 9 DOX loading (a) and releasing (b) efficiency of PBGs-1.

efficiencies of anti-tumour doxorubicin (DOX) in the PBGs were also studied in this article. As shown in Fig. 9, PBGs-1 could efficiently load 100 μg mL^{-1} DOX. The loading efficiency of the nanoparticles was 81.96 ± 1.22%. PBGs-1 had a high surface area (280.221 m^2 g^{-1}) and contained a large amount of nanopores, which provided enough space for PBGs to store small molecules in large amounts. The drug release was slow. At four days, the cumulative release of DOX in all PBGs-1 was still within 12%.

A CCK8 assay was used to analyse the inhibition effects of PBGs-1/DOX on Hela cells. After incubation with different final concentrations (10, 20, and 50 μg mL^{-1}) of PBGs-1/DOX for 48 h, the inhibitory activity of the nanoparticles was calculated. The results are shown in Fig. 10. There was a small increase in the Hela cells when they were treated with non DOX loading nanoparticles. However, PBGs/DOX nanoparticles demonstrated significant inhibition of proliferation in Hela cells. With an increase in the concentration, the cell inhibitory effect was more apparent. The proliferation of the Hela cells in the 50 μg mL^{-1} group changed significantly compared with untreated control cells or the 50 μg mL^{-1} non DOX loading PBGs. Live–dead cell staining showed similar results. After treating with 50 μg mL^{-1} PBGs/DOX, many cells became round, and some cells floated up (Fig. 11). The red PI staining also showed an increased number of dead cells compared with the control, 10 and 20 μg mL^{-1} groups (Fig. 11). Annexin V/PI apoptosis detection experiments exhibited remarkable effects of the 20 and 50 μg mL^{-1} groups (Fig. 12), which indicated that DOX could be successfully delivered into cells by PBGs.

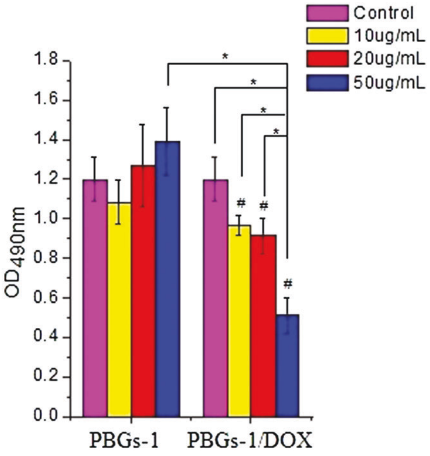

Fig. 10 Inhibition of PBGs-1–DOX on Hela cells detected by CCK8 (*$P < 0.01$, #$P < 0.01$ *vs.* control).

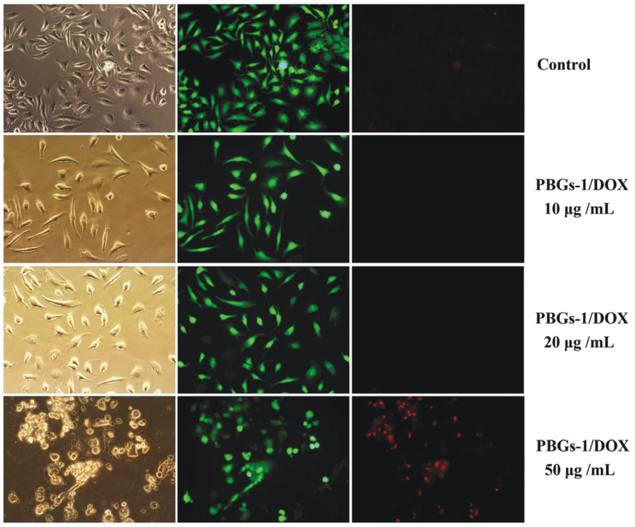

Fig. 11 Effect of PBGs-1/DOX on Hela cells detected by live–dead cell staining (200×). Left column: light microscopy; middle column: live cells; right column: dead cells.

The DOX-loaded PBGs demonstrated a significant antitumour effect by CCK8, live–dead cell staining and Annexin V/PI apoptosis experiments. The loading mechanism of the miR-7 and DOX was a little different. The loading and release properties of DOX, small molecular weight drugs, were mainly influenced by the specific surface area and pore morphology of the PBG nanoparticles, as well as the character of the molecules. As the physicochemical properties of microRNAs are different, they were negative charged, and they

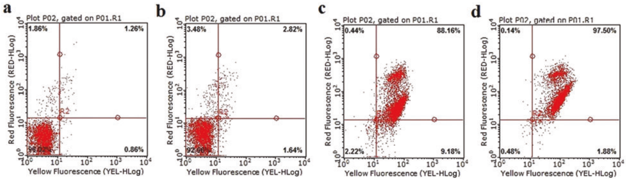

Fig. 12 Effect of PBGs-1/DOX on Hela cells detected by Annexin V/PI apoptosis experiments. (a) Control; (b–d) PBGs-1–DOX 10, 20 and 50 μg mL^{-1}.

were not only influenced by the above factors, but also by the zeta potential of the particles. Inspired by bionics, the PBGs that we fabricated were different from the traditional spherical nanoparticles. Although block copolymers and surfactant methods were introduced during the sol–gel process, increasing the CaO content resulted in irregular morphology of the particles from their natural state.[37] It is not easy to maintain the calcium concentration and the morphology of particles at the same time. Combining them with a sacrificial liquid template, the synthesised particles had a pinecone morphology. They had layered channels with the potential to load molecules, which was beneficial for controlling the release rate as well.

4 Conclusions

In this study, bio-inspired PBG nanoparticles were successfully synthesized using the sol–gel process combined with the aid of a soft template. The nanoparticles exhibited a pinecone-like morphology. Such novel nanoparticles could effectively load miR-7 and DOX and deliver them into cells successfully, resulting in an antitumour effect. The presented results indicate the potential of PBG nanoparticles as vectors for microRNA and drug delivery with higher efficiency.

Acknowledgements

This work was supported by the Natural Science Foundation of Guangdong Province (No. 2015A030310034), the Joint Funds of the National Natural Science Foundation of China (Grant No. U1501245), the National Natural Science Foundation of China (Grant No. 51602225), the Fundamental Research Funds for the Central Universities, and the Natural Science Foundation of Shandong Province (No. ZR2016HM05). S. Wang also acknowledges support from the National Science Foundation (CMMI 1634858) and a start up grant from Texas A&M University/TEES.

References

1 D. P. Bartel, *Cell*, 2009, **136**, 215–233.
2 M. Yang, Y. Li and R. W. Padgett, *Cytokine Growth Factor Rev.*, 2005, **16**, 387–393.
3 M. Inui, G. Martello and S. Piccolo, *Nat. Rev. Mol. Cell Biol.*, 2010, **11**, 252–263.
4 S. Yao, *Biol. Proced. Online*, 2016, **9**, 8.
5 K. R. Beavers, C. E. Nelson and C. L. Duvall, *Adv. Drug Delivery Rev.*, 2015, **88**, 123–137.
6 J. Raisch, A. Darfeuille-Michaud and H. T. Nguyen, *World J. Gastroenterol.*, 2013, **19**, 2985–2996.
7 A. Aigner and D. Fischer, *Pharmazie*, 2016, **71**, 27–34.
8 J. T. Mendell and E. N. Olson, *Cell*, 2012, **148**, 1172–1187.
9 J. K. Lam, M. Y. Chow, Y. Zhang and S. W. Leung, *Mol. Ther.–Nucleic Acids*, 2015, **4**, e252.
10 C. V. Pecot, F. A. Calin, R. L. Coleman, G. Lopez-Berestein and A. K. Sood, *Nat. Rev. Cancer*, 2011, **11**, 59–67.
11 L. L. Hench, R. J. Splinter, W. C. Allen and T. K. Greenlee, *J. Biomed. Mater. Res.*, 1971, **5**, 117–141.
12 H. Yu, J. Peng, Y. Xu, J. Chang and H. Li, *ACS Appl. Mater. Interfaces*, 2016, **8**, 703–715.
13 T. Wu, N. Cheng, C. Xu, W. Sun, C. Yu and B. Shi, *J. Biomed. Mater. Res., Part A*, 2016, **104**, 3004–3014.
14 S. Verrier, J. J. Blaker, V. Maquet, L. L. Hench and A. R. Boccaccini, *Biomaterials*, 2004, **25**, 3013–3021.
15 J. R. Jones, *Acta Biomater.*, 2015, **23**(Suppl), S53–S82.
16 W. Zhang, F. Zhao, D. Huang, X. Fu, X. Li and X. Chen, *ACS Appl. Mater. Interfaces*, 2016, **8**, 30747–30758.
17 R. Ravarian, X. Zhong, M. Barbeck, S. Ghanaati, C. J. Kirkpatrick, C. M. Murphy, A. Schindeler, W. Chrzanowski and F. Dehghani, *ACS Nano*, 2013, **7**, 8469–8483.
18 F. Zhao, W. Zhang, X. Fu, W. Xie and X. Chen, *RSC Adv.*, 2016, **6**, 91201–91208.
19 R. Brückner, M. Tylkowski, L. Hupa and D. S. Brauer, *J. Mater. Chem. B*, 2016, **4**, 3121–3134.
20 A. Hoppe, R. Meszaros, C. Stähli, S. Romeis, J. Schmidt, W. Peukert, B. Marelli, S. N. Nazhat, L. Wondraczek, J. Lao, E. Jallot and A. R. Boccaccini, *J. Mater. Chem. B*, 2013, **1**, 5659–5674.
21 Y. Shaharyar, E. Wein, J. J. Kim, R. E. Youngman, F. Muñoz, H. W. Kim, A. Tilocca and A. Goel, *J. Mater. Chem. B*, 2015, **3**, 9360–9373.
22 C. Wu and J. Chang, *J. Controlled Release*, 2014, **193**, 282–295.
23 L. L. Hench and J. R. Jones, *Front. Bioeng. Biotechnol.*, 2015, **3**, 194.
24 G. M. Luz and J. F. Mano, *J. Nanopart. Res.*, 2013, **15**, 1–11.
25 A. El-Fiqi, T. H. Kim, M. Kim, M. Eltohamy, J. E. Won, E. J. Lee and H. W. Kim, *Nanoscale*, 2012, **4**, 7475–7488.
26 Y. Xue, Y. Du, J. Yan, Z. Liu, P. X. Ma, X. Chen and B. Lei, *J. Mater. Chem. B*, 2015, **3**, 3831–3839.
27 C. T. Wu, W. Fan and J. Chang, *J. Mater. Chem. B*, 2013, **1**, 2710–2718.
28 X. Li, X. Chen, G. Miao, H. Liu, C. Mao, G. Yuan, Q. Liang, X. Shen, C. Ning and X. Fu, *J. Mater. Chem. B*, 2014, **2**, 7045–7054.
29 J. Luo, Y. Ling, X. Li, B. Yuan, F. Yu, W. Xie and X. Chen, *RSC Adv.*, 2015, **5**, 79239–79248.
30 Q. Liang, Q. Hu, G. Miao, B. Yuan and X. Chen, *Mater. Lett.*, 2015, **148**, 45–49.
31 B. Lei, X. Chen, X. Han and Z. Li, *J. Mater. Chem.*, 2011, **21**, 12725–12734.
32 Q. Hu, Y. Li, N. Zhao, C. Ning and X. Chen, *Mater. Lett.*, 2014, **134**, 130–133.

33 C. Mao, X. Chen, Q. Hu, G. Miao and C. Lin, *Mater. Sci. Eng., C*, 2016, **58**, 682–691.

34 Y. Li, Q. Hu, G. Miao, Q. Zhang, B. Yuan, Y. Zhu, X. Fu and X. Chen, *J. Biomed. Nanotechnol.*, 2016, **12**, 863–877.

35 Q. Hu, Y. Li, G. Miao, N. Zhao and X. Chen, *RSC Adv.*, 2014, **4**, 22678–22687.

36 I. Izquierdo-Barba, A. J. Salinas and M. Vallet-Regi, *Int. J. Appl. Glass Sci.*, 2013, **4**, 149–161.

37 S. Labbaf, O. Tsigkou, K. H. Müller, M. M. Stevens, A. E. Porter and J. R. Jones, *Biomaterials*, 2011, **32**, 1010–1018.

38 T. B. Hansen, J. Kjems and C. K. Damgaard, *Cancer Res.*, 2013, **73**, 5609–5612.

39 A. Hoppe, N. S. Güldal and A. R. Boccaccini, *Biomaterials*, 2011, **32**, 2757–2774.

40 I. D. Xynos, A. J. Edgar, L. D. Buttery, L. L. Hench and J. M. Polak, *Biochem. Biophys. Res. Commun.*, 2000, **276**, 461–465.